Probing isoscalar giant resonances with multipolarity $L \leqslant 3$ in even-A neodymium isotopes

M. Abdullah,[1] K. Khokhar,[1] S. Bagchi,[1,*] M. N. Harakeh,[2] H. Akimune,[3] D. Das,[1,†] T. Doi,[4] L. M. Donaldson,[5] Y. Fujikawa,[4] M. Fujiwara,[6] T. Furuno,[7,8] U. Garg,[9] Y. K. Gupta,[10,11] K. B. Howard,[9] Y. Hijikata,[4] K. Inaba,[4] S. Ishida,[12] M. Itoh,[12] N. Kalantar-Nayestanaki,[2] D. Kar,[1] T. Kawabata,[7] S. Kawashima,[3] K. Kitamura,[3] N. Kobayashi,[6] Y. Matsuda,[3,12] A. Nakagawa,[12] S. Nakamura,[6] K. Nosaka,[3,12] S. Okamoto,[4] S. Ota,[6] S. Pal,[1] R. Pramanik,[1,‡] S. Roy,[1,§] S. Weyhmiller,[9,‖] Z. Yang,[6] and J. C. Zamora[13]

[1]*Department of Physics, IIT-ISM Dhanbad, Jharkhand 826004, India*
[2]*Nuclear Energy Group, ESRIG, University of Groningen, 9747 AA Groningen, The Netherlands*
[3]*Department of Physics, Konan University, Hyogo 658-8501, Japan*
[4]*Department of Physics, Kyoto University, Kyoto 606-8502, Japan*
[5]*iThemba LABS, Somerset West, 7129, South Africa*
[6]*Research Center for Nuclear Physics, Osaka University, Osaka 567-0047, Japan*
[7]*Department of Physics, Osaka University, Toyonaka, Osaka 560-0043, Japan*
[8]*Department of Applied Physics, University of Fukui, Fukui 910-8507, Japan*
[9]*Department of Physics, University of Notre Dame, Notre Dame, Indiana 46556, USA*
[10]*Nuclear Physics Division, Bhabha Atomic Research Centre, Mumbai 400085, India*
[11]*Homi Bhabha National Institute, Anushaktinagar, Mumbai 400094, India*
[12]*Cyclotron and Radioisotope Center, Tohoku University, Sendai 980-8578, Japan*
[13]*Facility for Rare Isotope Beams, Michigan State University, East Lansing, Michigan 48824, USA*

(Received 11 May 2025; accepted 12 September 2025; published 21 October 2025)

Background-free inelastic-scattering spectra were measured for even-A neodymium (Nd) isotopes using a halo-free 386-MeV α beam at forward angles, including 0°, to examine the influence of deformation on isoscalar giant resonances. The strength distributions of isoscalar giant resonances (with multipolarity $L \leqslant 3$) in ^{142}Nd and $^{146-150}$Nd isotopes are determined using multipole decomposition analysis. This analysis is based on angular distributions calculated within the framework of the distorted-wave Born approximation with transition densities generated with a Woods-Saxon type potential. The isoscalar giant monopole resonance exhibits a distinct splitting into low-energy and high-energy components while going from the spherical nucleus ^{142}Nd to the well-deformed nucleus ^{150}Nd due to coupling with the $K = 0$ component of the isoscalar giant quadrupole resonance (ISGQR). The isoscalar giant dipole resonance displays a bimodal structure, with an evidence of coupling between the dipole ($E1$) and high-energy octupole ($E3$) resonance due to deformation effects. The ISGQR splits into distinct K components ($K = 0$, 1, and 2) due to deformation. A signature of an overtone mode in ISGQR at an energy around 26 MeV has been obtained.

DOI: 10.1103/1p1h-5jh2

I. INTRODUCTION

Giant resonances are manifestations of the collective excitation of nucleons within a nucleus, arising from transitions between the ground state and the collective excited states [1]. The nucleus oscillates, in the excited state, around a mean shape or density depending on the change in the spin, isospin, and the angular momentum quantum number. Among the various giant-resonance modes, the isoscalar giant monopole resonance (ISGMR) and isoscalar giant dipole resonance (ISGDR) are particularly significant, as their excitation energies are directly related to the incompressibility of the finite nucleus (K_A). Consequently, they are also referred to as compression modes [1]. From the measured K_A, the incompressibility of infinite nuclear matter (K_∞) can be deduced through microscopic calculations [2–4]. The incompressibility of infinite nuclear matter at the saturation density plays a crucial role in mean-field models of nuclear many-body systems and in the dynamics of high-density astrophysical objects and supernova explosions [5–9].

Isoscalar giant resonances have been extensively studied in spherical nuclei. However, the experimental data for deformed nuclei are scarce. The effects of deformation on the isovector giant dipole resonance (IVGDR) have been thoroughly investigated by studying the photoneutron cross section and comparing experimental results for spherical and deformed

*Contact author: sbagchi@iitism.ac.in
†Present address: TU Darmstadt and GSI Helmholtzzentrum, Germany.
‡Present address: IIT Guwahati, India.
§Present address: IIT Roorkee, India.
‖Present address: Yale University, USA.

nuclei [10], including Nd isotopes [11]. In deformed nuclei, the strength distribution of the IVGDR exhibits a splitting attributed to the different oscillation frequencies along the short and long axes. It is noteworthy that the IVGDR in both spherical and deformed Nd isotopes, as well as in ^{152}Sm, has also been studied through inelastic proton scattering [12,13]. Additionally, the IVGDR in Nd isotopes has been explored using a translational and Galilean invariant quasiparticle random-phase approximation (QRPA) method [14].

Isoscalar giant resonances have been explored in spherical and deformed Sm isotopes [15–17], the fission decay of ^{238}U [18], and lighter nuclei such as ^{24}Mg [19] and ^{28}Si [20]. Recently, we reported [21] on both the ISGMR and isoscalar giant quadrupole resonance (ISGQR) and their strength distributions in Nd isotopes, spanning from spherical ^{142}Nd to deformed ^{150}Nd. Notably, earlier studies of isoscalar giant resonances in Nd isotopes at a much lower α-particle bombarding energy of 129 MeV [22] did not extract the strength distributions of these resonances. In deformed nuclei, the strength distribution of an isoscalar giant resonance splits into different K components, where K, the projection onto the symmetry axis, is a good quantum number. In the case of the ISGMR, the strength distribution splits into low-energy (LE) and high-energy (HE) components due to coupling with the $K = 0$ component of the ISGQR [23]. In the case of the ISGQR, the strength distribution splits into three K components ($K = 0$, 1, and 2) [24]. The splitting of the strength distribution of the ISGQR is reflected in the broadening of the resonance width [16,25]. Investigations of the ISGMR in deformed ^{154}Sm, conducted both at the Research Center for Nuclear Physics (RCNP) [15] and Texas A&M University (TAMU) [17], using inelastic α-particle scattering, have yielded contradictory results. A strong splitting of the ISGMR strength in ^{154}Sm with a pronounced low-energy peak was observed in the TAMU data, indicating significant splitting, which was not the case for the RCNP data.

A "bimodal" strength distribution for the ISGDR has been observed in medium- to heavy-mass nuclei [16,17,26–28]. While the HE component of this bimodal ISGDR distribution remains largely unchanged, the width and energy-weighted sum rule (EWSR) of the LE component increases with increasing deformation in Sm isotopes [16]. The strength distribution of the high-energy octupole resonance (HEOR) also appears to be affected by nuclear deformation, as noted in Refs. [16,29]. However, in Ref. [29], the ISGDR was not separated from the HEOR, as both resonances occur at similar excitation energies. The negative-parity isoscalar resonances, i.e., ISGDR (1^-) and HEOR (3^-), couple in the $K^\pi = 0^-$ and 1^- channels as predicted by QRPA calculations within the basis of the Skyrme energy-density functional [25] and by the fluid-dynamical method based on the generalized scaling approximation [30]. Experimental evidence of this predicted coupling has been observed in Sm isotopes, where an enhancement of the low-energy component of the ISGDR has been accompanied by a shift in the HEOR strength towards lower excitation energies [16].

Isoscalar giant resonances with multipolarity $L \geqslant 2$ are primarily associated with the first-order term of the transition operator, often referred to as the "main tone" of the transition operator. However, the first-order term of the transition operator for the ISGMR is a constant and that for the ISGDR is associated with the spurious center-of-mass motion. As a result, the second-order terms of the transition operators, representing the "overtone" modes, become relevant for both the ISGMR and ISGDR [1,3]. Since the excitation energies of the ISGMR and ISGDR are directly related to the nuclear incompressibility of finite nuclei, the "overtone" modes are related to K_A. Overtone modes of isoscalar giant resonances with multipolarities $L \geqslant 2$ remained elusive until the first evidence of a high-lying resonance with $L = 2$ characteristics was found at around 27 MeV during the investigation of the direct proton decay from the ISGDR state in ^{208}Pb [31]. It was also confirmed later from the neutron decay of the ISGDR state in ^{208}Pb [32]. This high-order mode in the ISGQR, referred to as ISGQR2, corresponds to a $4\hbar\omega$ excitation and refers to another compression mode in addition to the ISGMR and ISGDR. Recent results from studies on Nd isotopes have also confirmed the presence of this overtone mode, providing further evidence of its existence [21].

In a previous study [21], we reported the strength distributions of the ISGMR, ISGQR, and ISGQR2 in even-A $^{142,146-150}$Nd, where the nuclear deformation increases from the nearly spherical ^{142}Nd [$\beta_2 = 0.0916(8)$] to more deformed ^{150}Nd [$\beta_2 = 0.285(3)$] [33]. In this paper, we provide a systematic study of isoscalar giant resonances up to $L = 3$ in these Nd isotopes.

II. EXPERIMENTAL SETUP

For the present study on isoscalar modes of giant resonances, the α-particle probe was an excellent choice since its spin and isospin are zero. Inelastic α-particle scattering off ^{142,146,148,150}Nd isotopes was measured at the RCNP, Osaka University, Japan. A halo-free ^{4}He^{++} beam with an energy of 386 MeV, was transported toward the experimental area through the west-south beamline after a single-turn extraction from the ring cyclotron. This ^{4}He^{++} beam then impinged on self-supporting ^{142,146,148,150}Nd targets enriched to values greater than 95% with areal densities varying between 4.5 and 5.0 mg/cm^2. At this beam energy, the knock-out and pick-up reaction probabilities are low, and the predominant influence arises from single-step reactions [34]. The high-resolution magnetic spectrometer "Grand Raiden" (GR) was used to analyze the momentum of inelastically scattered α particles [35]. The energy resolution achieved was around 175 keV, a level of precision deemed adequate for investigating the giant resonances having widths of approximately 2–3 MeV. The beam current, which ranged from 0.1 to 10 nA, was restricted by the data acquisition rate and the maximum current available from the accelerator.

A focal-plane detector system consisting of a pair of plastic scintillators and position-sensitive multiwire drift chambers was used to observe the horizontal and vertical positions of inelastically scattered α particles, allowing particle identification and reconstruction of trajectories of the scattered particle.

Figure 1(a) shows the typical particle identification plot at 0° for the GR spectrometer, which corresponds to an average angle of $\theta_{avg} = 0.75°$. The spectrometer was operated

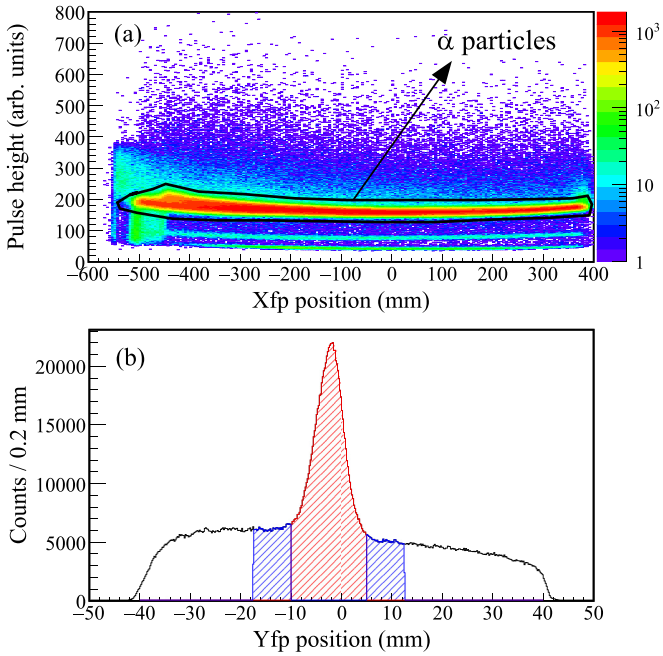

FIG. 1. (a) Particle identification spectrum for α particles inelastically scattered from ^{142}Nd: energy deposited in the first plastic scintillator detectors against the horizontal focal-plane position ($X_{\rm fp}$). The gated events, enclosed by the black solid line, correspond to the inelastically scattered α particles. (b) The vertical-position spectrum ($Y_{\rm fp}$) of α particle scattered from ^{142}Nd at 0° is shown, along with the focusing in the Y direction. The red-hatched region includes both true and background events, while the blue-hatched regions represent background events only.

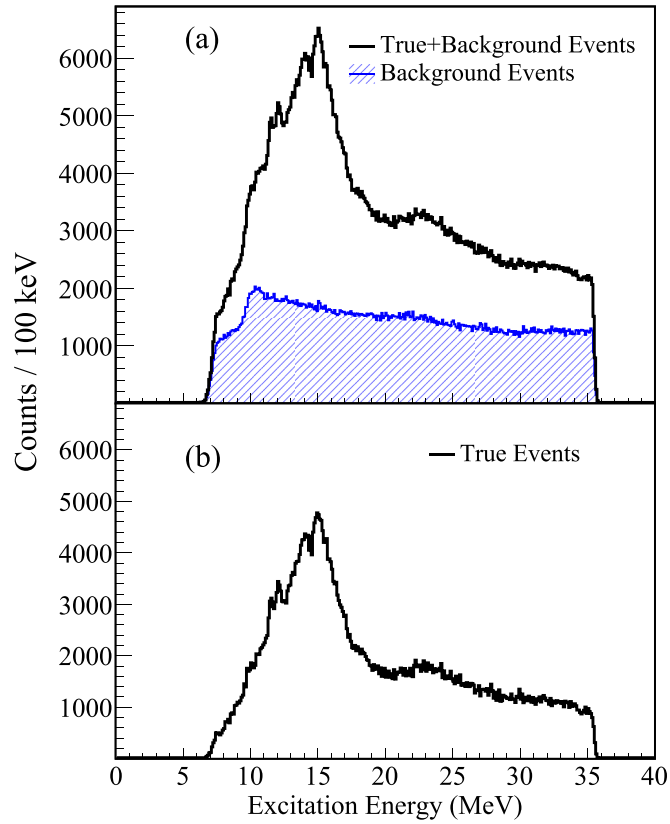

FIG. 2. (a) Excitation-energy spectrum for ^{142}Nd(α, α') reaction at $\theta_{\rm GR} = 0°$ ($\theta_{\rm avg} = 0.75°$) after particle identification, ion-optical corrections, and energy calibration. The black line shows the total true + background events and the blue-hatched region shows the instrumental background events. (b) The black histogram shows the true events after instrumental background subtraction.

in double-focusing mode, where true events resulting from scattering off the target are focused into a narrow band along the vertical plane [indicated by the red-hatched region in Fig. 1(b)]. The events originating from the instrumental background are either overfocused or underfocused in the vertical plane, as shown by the blue-hatched regions in Fig. 1(b). By subtracting background events located at the off-median focal-plane positions from those at the median focal-plane position, the instrumental background can be efficiently eliminated [35]. In Fig. 2(a), the excitation-energy spectrum of ^{142}Nd is shown for the 0° GR angle, where the blue-hatched regions shows the instrumental background that corresponds to the sum of blue-hatched regions in Fig. 1(b). Figure 2(b) displays the result of subtracting the background events from the total events in order to isolate the true inelastically scattered events.

The inelastic scattering of α particles was measured at forward angles, $0° \leqslant \theta_{\rm Lab} \leqslant 10°$, where the angular distributions are characteristic of different multipolarities. To determine the optical-model parameters (OMPs), however, elastic scattering on ^{142}Nd was measured over a wide angular range from 3.5° to 20.5°. To calibrate the Nd excitation-energy spectra, inelastic α scattering on a ^{24}Mg target (with an areal density of 2.5 mg/cm^2) was measured at the same spectrometer angles as those used for the Nd targets. For ion-optical correction, a sieve slit (a multihole aperture with holes separated horizontally by 5 mm and vertically by 12 mm) was placed between the target and the first magnet of the spectrometer. The sieve slit effectively divides the scattered particle stream into small pencil beams, allowing the determination of both horizontal and vertical scattering angles at the target. By analyzing such sieve-slit data, the relationship between the position and angle of incidence at the focal plane and the corresponding scattering angles at the target can be deduced.

III. DATA ANALYSIS

A. Determination of optical-model parameters from elastic-scattering data

An optical model employs a complex scattering potential to describe the nuclear scattering. It provides an interpretation of elastic scattering in terms of the scattering potential and the associated wave function for the relative motion of the target and projectile, which could be used to study the inelastic scattering. For this purpose, the cross section data of α elastic scattering on ^{142}Nd was analyzed over a wide angular range of 3.5° to 20.5°. A Woods-Saxon type potential has been used for both real and imaginary parts of the complex optical potential with the following functional form:

$$V(r) = -V_r \cdot F(R_r, a_r) - iV_i \cdot F(R_i, a_i), \qquad (1)$$

TABLE I. Optical-model parameters from χ^2 minimization of ^{142}Nd elastic-scattering data [36].

E_α (MeV)	V_r (MeV)	V_i (MeV)	R_r (fm)	R_i (fm)	a_r (fm)	a_i (fm)
386	79.24	26.01	6.61	7.56	0.792	0.625

where V_r is the attractive real potential, V_i is the absorptive imaginary potential and

$$F(R,a) = \left[1 + \exp\left(\frac{r-R}{a}\right)\right]^{-1}, \quad (2)$$

where R_r (R_i) is the real (imaginary) radius of the nuclear potential and a_r (a_i) is the real (imaginary) part of the diffuseness of the potential. The OMPs are derived through a χ^2 minimization by fitting the angular distribution for ^{142}Nd(α,α) elastic scattering. We have used brute-force and basin-hopping global optimization techniques using Python for χ^2 minimization [36]. The angular distributions, including elastic and inelastic scattering, were calculated within the framework of the distorted-wave Born approximation (DWBA) using the coupled-channel code CHUCK3 [37]. During the minimization process, the newly optimized parameters obtained in each iteration were fed into the CHUCK3 code to compute the angular distribution of elastic α scattering, which was then utilized for further minimization. Unfortunately, due to limited beam time, α elastic-scattering data for ^{146,148,150}Nd were unavailable. Consequently, the OMPs derived from the ^{142}Nd data were employed in the DWBA calculations for these isotopes. Using OMPs from a nearby nucleus or isotope introduces negligible variations in the extraction of strength distributions of giant resonances [38–40]. Moreover, OMPs derived for spherical nuclei have been effectively utilized to determine strength distributions in deformed nuclei without significantly altering their expected characteristics [15,16]. Table I summarizes the fitting parameters obtained from the χ^2 minimization, whereas Fig. 3(a) shows the angular distribution of α elastic scattering on ^{142}Nd along with the fit.

In ^{142}Nd, the angular distributions for the states at 1.575 MeV ($J^\pi = 2^+$) and 2.083 MeV ($J^\pi = 3^-$) have been calculated within the DWBA framework by using the obtained OMPs and the known $B(E2) = 0.265(13)\ e^2\,\mathrm{b}^2$ [33,41] and $B(E3) = 0.44(22)\ e^2\,\mathrm{b}^3$ [42] values. They show good agreement with the experimental data, as illustrated in Figs. 3(b) and 3(c), respectively, demonstrating the reliability of the derived OMPs. The angular distribution of the $J^\pi = 2^+$ state of ^{148}Nd at 0.301 MeV, calculated using the same OMPs listed in Table I, is shown in Fig. 3(b) with dashed lines. The maxima and minima of the 2^+ angular distribution for ^{148}Nd agree reasonably well with those of ^{142}Nd. The observed difference in the cross sections originates from the difference in the $B(E2)$ values, with the $B(E2)$ for the first 2^+ state at 0.301 MeV in ^{148}Nd being $1.37(2)\ e^2\,\mathrm{b}^2$ [33]. Furthermore, the calculated elastic α angular distribution for ^{144}Sm using the OMPs presented in Table I, agrees well with the elastic-scattering data from Ref. [16]. This reinforces the accuracy of the derived optical potential parameters.

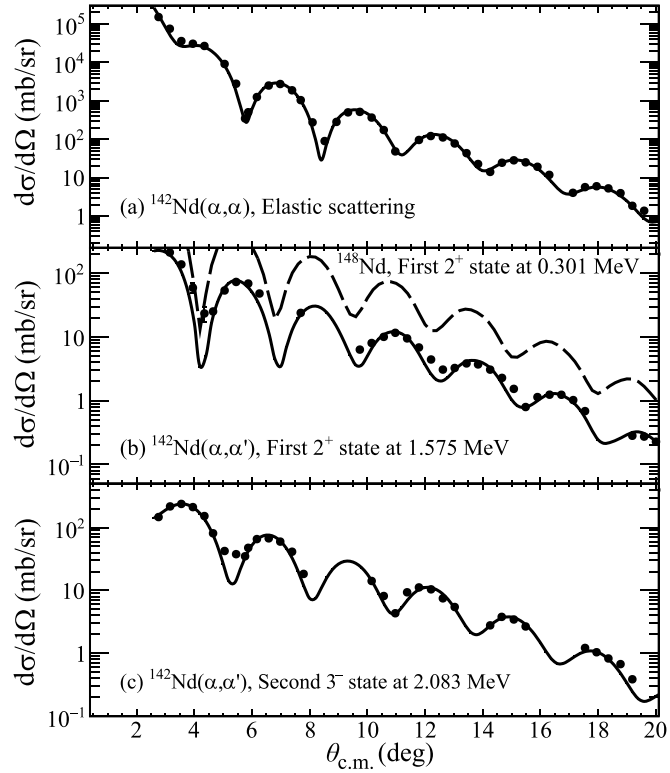

FIG. 3. (a) Differential cross sections of elastic α-particle scattering from ^{142}Nd at 386 MeV. The closed black circles show the measured cross sections. The solid line shows the optical-model fit to the data [36]. Angular distribution of differential cross sections for (b) the 1.575 MeV 2^+ state and (c) the 2.083 MeV 3^- state in ^{142}Nd. The solid lines in (b) and (c) show the result of the DWBA calculation (see text). The absence of certain data points in (b) and (c) is attributed to contamination from oxygen and hydrogen (see Sec. III C). The angular distribution of the first 2^+ state of ^{148}Nd at 0.301 MeV is shown in (b) with dashed lines.

B. Calibration of excitation-energy spectra using inelastic α scattering on ^{24}Mg

To calibrate the focal-plane detector, high-resolution ^{24}Mg(α,α') data [43] were utilized due to the well-characterized low-lying discrete states of ^{24}Mg. The measurements were performed at the same GR spectrometer angles (0°, 2.5°, 3.5°, 5°, 6.5°, 8°, and 9.5°) as those used for the Nd targets. Since the Nd isotopes are significantly heavier than ^{24}Mg, a direct conversion of the horizontal focal-plane position spectra into excitation energy was not feasible. Instead, the high-resolution excitation-energy spectra obtained from the ^{24}Mg(α,α') data [43] were converted into scattered α-particle momentum spectra using the kinematic relationship between the incident α-particle momentum and the excitation energy of the recoiling ^{24}Mg target nucleus. The measured horizontal focal-plane position spectra from the present experiment were then calibrated by comparing them to the momentum spectra at each GR spectrometer

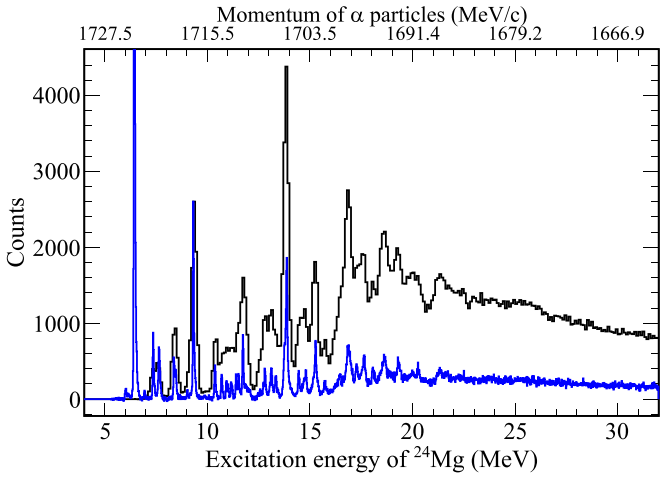

FIG. 4. The 0° calibration spectrum (black histogram) for ^{24}Mg(α, α') obtained at an α energy of 386 MeV, showing both the calibrated excitation energy of ^{24}Mg (bottom horizontal axis) as well as the momentum of the scattered α particle (top horizontal axis). The high-resolution ^{24}Mg(α, α') spectrum from Ref. [43], also measured at 0° GR angle and shown as the blue histogram, was used for calibration. An arbitrary normalization factor of 1.43 has been applied to the blue histogram to match the peak height at 9.3 MeV with that of the experimental data.

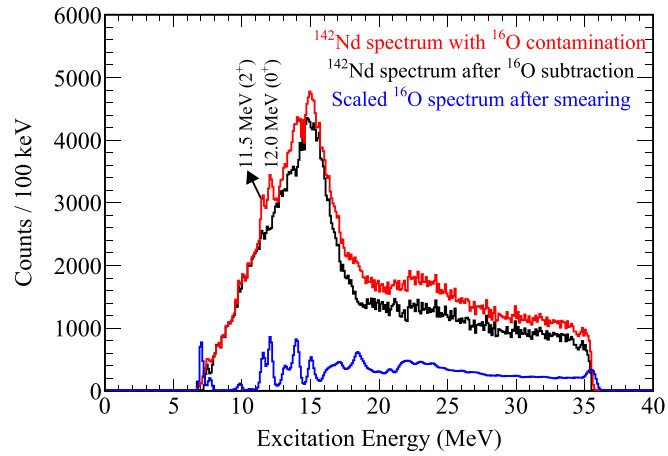

FIG. 5. The excitation-energy spectrum of ^{142}Nd including the ^{16}O contamination is shown in red. The reference oxygen spectrum taken from Ref. [44] (resolution matched) is shown in blue. Both datasets were taken at $\theta_{GR} = 0°$ ($\theta_{avg} = 0.75°$). The excitation-energy spectrum of ^{142}Nd after subtraction of the oxygen contamination is shown in black.

angle. These calibration parameters were subsequently used to convert the horizontal focal-plane position spectra obtained from α-particle inelastic scattering on Nd targets into the corresponding scattered α-particle momentum spectra. Finally, these α-particle momentum spectra for the Nd isotopes were converted into excitation-energy spectra through kinematics calculations. Figure 4 illustrates a calibration spectrum (black histogram) for ^{24}Mg at 0° GR angle including the reference spectrum at 0° GR angle (blue histogram) from Ref. [43]. The excellent agreement between the two histograms after an arbitrary normalization confirms the reliability of the calibration procedure.

C. Subtraction of hydrogen and oxygen contamination

The Nd targets are prone to hydrolysis, resulting in significant contamination from oxygen and hydrogen in each Nd isotope. In the case of hydrogen contamination, only elastic proton scattering with α particles needs to be considered, as there are no collective structures to excite. Elastic scattering off protons exhibits a significantly larger cross section compared to the inelastic excitations of the Nd target nuclei. Consequently, hydrogen contamination can be removed by excluding the affected data points during offline analysis, as illustrated by the missing data points in the angular distributions shown in Fig. 3 and Fig. 7. The missing data points in Figs. 3(b) and 3(c) also account for oxygen contamination.

To eliminate oxygen contamination, high-resolution ^{16}O(α, α') measurements performed at the same beam energy at RCNP [44] were utilized. The excited states of ^{16}O, such as the peaks at 11.520 MeV (2^+) and 12.049 MeV (0^+), extend into the giant-resonance region of the Nd isotopes, as shown in Fig. 5 with the red histogram. After aligning the kinematics with the measured excitation energies of the Nd inelastic spectra, the oxygen excitation-energy spectra were smeared with a Gaussian function with a width of around 140 keV to match the experimental resolution. These smeared spectra were subsequently scaled by the ratio of the integrals of the prominent oxygen peaks in the Nd excitation-energy spectra to those in the kinematically transformed oxygen spectra resulting in the blue spectrum in Fig. 5. Finally, the scaled oxygen spectra were subtracted from the Nd excitation-energy spectra to eliminate oxygen contamination giving the black spectrum in Fig. 5.

The excitation-energy spectra for all Nd isotopes, after particle identification, ion-optical correction and subtraction of the instrumental background and contamination, are presented in Fig. 6 for 0° GR angle. As evident from Fig. 6, the excitation energy spectra progressively broaden with increasing nuclear deformation from ^{142}Nd to ^{150}Nd, reflecting a clear splitting of the strength distributions.

D. Transition densities, multipole decomposition analysis, strength distributions and moments

The transition densities are computed and expressed in terms of ground-state densities and they are estimated utilizing the methods described in Ref. [45] for the monopole ($L = 0$) transition and in Ref. [46] for the dipole ($L = 1$) transition. The transition densities for $L \geqslant 2$ are derived from the surface oscillation. Reference [1] provides a detailed description of the transition densities and sum rules for various multipolarities. The transition densities of $L \geqslant 2$ multipoles are given by:

$$\rho^{(L\geqslant 2)}(r) = -\frac{\beta_{L\geqslant 2} R}{\sqrt{2L+1}} \frac{d}{dr} \rho_0(r) \tag{3}$$

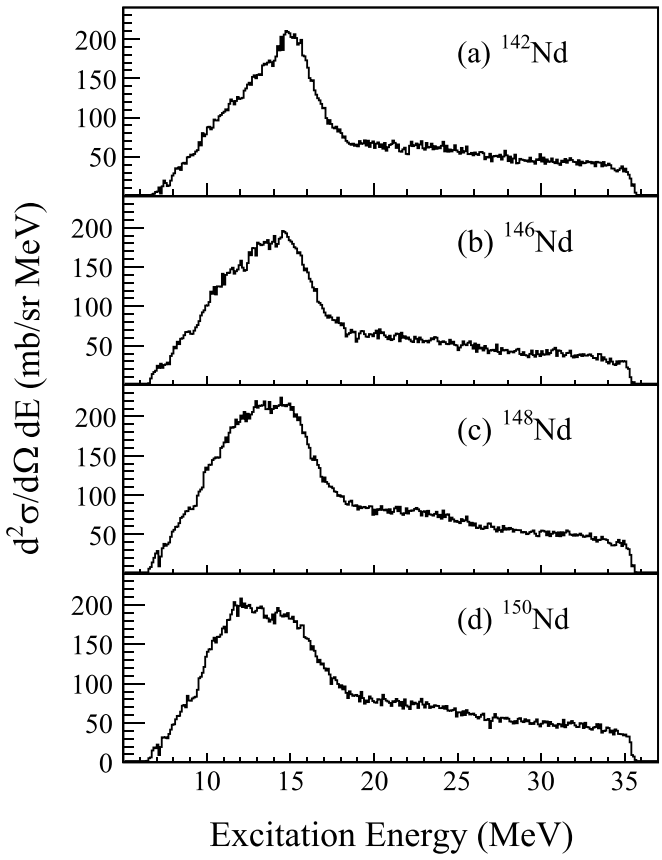

FIG. 6. Measured double-differential cross sections for the Nd isotopes at $\theta_{\rm avg} = 0.75^\circ$ after particle identification, subtraction of the instrumental background, ion-optical correction, and subtraction of contaminants.

with

$$\beta^2_{L\geqslant 2} = (2L+1)\frac{\hbar\omega_L}{2C_L}, \tag{4}$$

where $\hbar\omega_L$ is the energy of each phonon, and C_L is the restoring force parameter, and they are obtained following the procedure mentioned in Refs. [1,47]. β_L is the collective coupling parameter of isoscalar L-pole giant resonances considering surface oscillations.

The transition density for a dipole is given by:

$$\rho^{(1)}(r) = -\frac{\beta_1}{R\sqrt{3}}\Bigg[3r^2\frac{d}{dr} + 10r - \frac{5}{3}\langle r^2\rangle\frac{d}{dr} + \epsilon\left(r\frac{d^2}{dr^2} + 4\frac{d}{dr}\right)\Bigg]\rho_0(r), \tag{5}$$

where

$$\beta^2_1 = \frac{2\pi\hbar^2}{mAE_x}\frac{3R^2}{\left[11\langle r^4\rangle - \frac{25}{3}\langle r^2\rangle^2 - 10\epsilon\langle r^2\rangle\right]}. \tag{6}$$

The transition density for a monopole can be expressed as:

$$\rho^{(0)}(r) = -\beta_0\left[3 + r\frac{d}{dr}\right]\rho_0(r) \tag{7}$$

with

$$\beta^2_0 = \frac{2\pi\hbar^2}{mAE_x}\frac{1}{\langle r^2\rangle}, \tag{8}$$

where R is the half-density radius of the Fermi mass distribution, m is the mass of the nucleon, A is the mass number, E_x is the excitation energy, $\langle r^L\rangle$ is the radial moment of the density of the ground state, and β_1 and β_0 are the collective coupling parameters for the isoscalar dipole and monopole resonances, respectively. The parameter ϵ is expressed as $(4/E_2 + 5/E_0)\hbar^2/3mA$, where $E_2 = 65A^{-1/3}$ and $E_0 = 80A^{-1/3}$.

Isoscalar giant resonances are predominantly excited by the scalar, isoscalar α-particle probe. However, it is important to note that Coulomb excitation can also induce isovector modes. As a result, the IVGDR mode can be excited with a non-negligible cross section by inelastic α-particle scattering. To accurately extract the strength distribution of the isoscalar giant resonances, the contribution from the IVGDR must be carefully subtracted before performing multipole decomposition analysis (MDA). The transition density of the IVGDR mode can be expressed as [1]:

$$\rho^{(1)}_{IV}(r) = -\alpha_1\gamma\frac{N-Z}{A}\left[\frac{d}{dr} + \frac{1}{3}R_u\frac{d^2}{dr^2}\right]\rho_0(r) \tag{9}$$

with

$$\alpha^2_1 = \frac{\pi\hbar^2}{2m}\frac{A}{NZE_x}, \tag{10}$$

where $\gamma = \frac{3(R_n - R_p)A}{2R_u(N-Z)}$ and R_n, R_p, and R_u are the half-density radii of the neutron, proton, and nucleon distributions, respectively. The form factors for the IVGDR were obtained using the Goldhaber-Teller model [45,48], and the available photoneutron data [49] for Nd isotopes were used to estimate the exhausted sum rules.

The Nd(α,α') excitation-energy spectra were divided into 1-MeV energy bins to minimize statistical fluctuations. The strengths corresponding to various multipolarities were extracted using the MDA method. This method involves fitting the experimental differential cross section at each excitation energy with a linear combination of angular distributions calculated within the DWBA framework for different multipolarities as demonstrated in Eq. (11):

$$\frac{d^2\sigma^{\rm exp}(\theta_{\rm CM}, E_x)}{d\Omega dE} = \sum_{L=0}^{7} A_L(E_x)\frac{d^2\sigma^{\rm DWBA}_L(\theta_{\rm CM}, E_x)}{d\Omega dE}. \tag{11}$$

The $A_L(E_x)$ coefficients show the fraction of the EWSR for a particular energy bin for multipolarity L. Only multipoles up to $L = 7$ have been considered in this analysis. The cross sections calculated under the DWBA framework using the CHUCK3 code [37] correspond to 100% EWSR for a given excitation energy E_x. At higher excitation energies, the physical continuum predominates, and at larger angles, cross sections decrease while the angular distributions become featureless. As a result, giant-resonance strength distributions could be reliably extracted only up to $L = 3$. Before fitting the experimental data, the calculated angular distributions for $L \geqslant 4$ were summed. The coefficients $A_L(E_x)$ for different

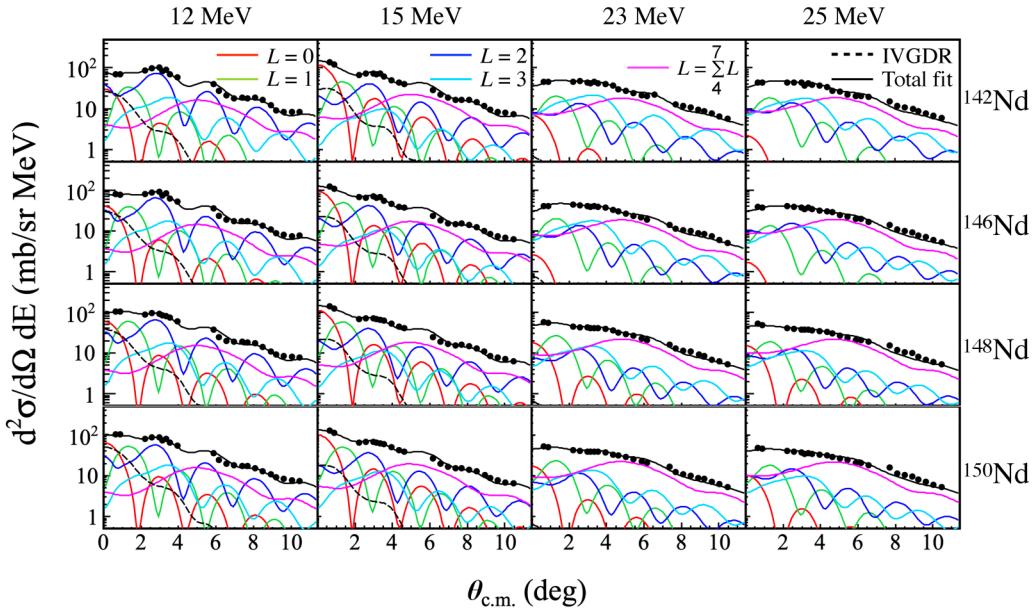

FIG. 7. Multipole-decomposition analyses for ^{142,146,148,150}Nd are shown for excitation-energy bins centered at 12, 15, 23, and 25 MeV. Solid black lines represent the total fits to the data points. Fitted contributions are also shown from the isoscalar monopole (red), dipole (green), quadrupole (blue), octupole (cyan), and higher multipole modes (magenta). The contributions from the IVGDR, determined through known photoneutron cross-section data and the Goldhaber-Teller model, are also depicted by dashed lines.

multipoles were determined using χ^2 minimization. The coefficients were eventually related to the fraction of EWSR. Once the fitting parameters were obtained, the uncertainty associated with each parameter was obtained by fitting the data again and fixing all other parameters except the parameter of interest, thus raising the confidence level by 68%. Typical results of the MDA at excitation energies of 12, 15, 23, and 25 MeV are presented in Fig. 7.

Using the coefficients A_L, the strength distributions for monopole ($L = 0$), dipole ($L = 1$), and higher-order multipolarities ($L \geqslant 2$) were obtained using Eqs. (12), (13), and (14), respectively:

$$S_0(E_x) = \frac{\hbar^2}{2m}\frac{Z^2}{A}\frac{\langle r^2\rangle}{E_x}A_0(E_x), \tag{12}$$

$$S_1(E_x) = \frac{\hbar^2}{8\pi m}\frac{3}{4}\frac{Z^2}{A}\left(\frac{11\langle r^4\rangle - \frac{25}{3}\langle r^2\rangle^2 - 10\epsilon\langle r^2\rangle}{E_x}\right)A_1(E_x), \tag{13}$$

$$S_L(E_x) = \frac{\hbar^2}{8\pi m}L(2L+1)^2\frac{Z^2}{A}\frac{\langle r^{2L-2}\rangle}{E_x}A_L(E_x), \tag{14}$$

where Z and A denote the atomic number and mass number of the nucleus, respectively; the other definitions of the symbols have been defined earlier. The kth moment of the strength function is defined as:

$$m_k = \int S_L(E_x)E_x^k\,dE_x, \tag{15}$$

where m_k is the kth moment and E_x is the excitation energy. The centroid of the strength distribution of giant resonances is associated with different moment ratios across various model frameworks. In the scaling, constrained, and centroid models, the excitation energy of the multipole strength distribution is traditionally defined by the moment ratios $\sqrt{m_3/m_1}$, $\sqrt{m_1/m_{-1}}$, and m_1/m_0, respectively [50].

IV. RESULTS AND DISCUSSION

A. ISGMR

The ISGMR strength distributions of the Nd isotopes (^{142,146,148,150}Nd) exhibit a distinct splitting into two components—LE and HE as one moves from the nearly spherical ^{142}Nd [$\beta_2 = 0.0916(8)$] to the more deformed, prolate-shaped ^{150}Nd [$\beta_2 = 0.285(3)$] [33]. This splitting arises due to coupling of the ISGMR with the $K = 0$ component of the ISGQR. The transition operator for monopole transition is given as follows:

$$O^{00} = \frac{Z}{2A}\sum_k r_k^2, \tag{16}$$

where the sum is over all the nucleons. The factor $\frac{Z}{A}$ is used for truly collective isoscalar transitions where all the nucleons in the nucleus participate in the collective motion [1]. This is a second-order expansion (overtone mode) of the spherical Bessel function since the first-order term does not induce the intrinsic excitation of the nucleus as it is a constant. Figure 8 shows the ISGMR strength distributions for these Nd isotopes, obtained using Eq. (12). For the spherical nucleus ^{142}Nd, the extracted strength distribution is well described by a single Lorentzian function. For the deformed ^{146,148,150}Nd isotopes, the strength distributions are fitted with a double Lorentzian function. The Lorentzian function used for the fits is given as

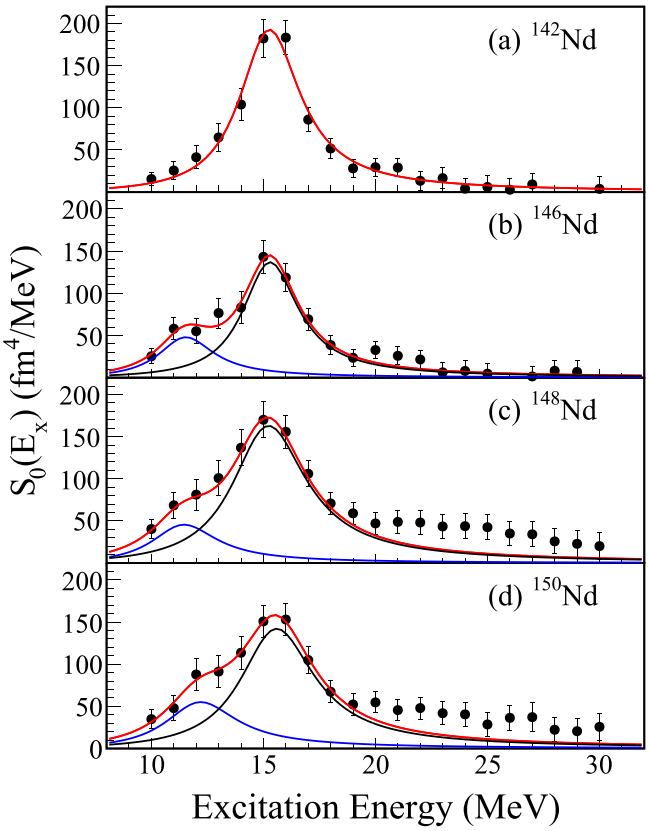

FIG. 8. The ISGMR strength distributions for $^{142-150}$Nd obtained from the MDA. The red lines show the results of single-Lorentzian fitting in (a) ^{142}Nd, and of double-Lorentzian fitting in (b) ^{146}Nd, (c) ^{148}Nd, and (d) ^{150}Nd. In deformed Nd isotopes, the LE and HE components of the ISGMR are indicated by blue and black lines, respectively.

follows [51]:

$$S_L(E_x) = \frac{S_p}{1 + \left(E_x^2 - E_p^2\right)^2 / E_x^2 \Gamma^2}. \tag{17}$$

Here S_p represents the strength of the Lorentzian function at the peak energy, E_p is the peak energy, E_x denotes the excitation energy, and Γ is the width of the Lorentzian function. We performed the Lorentzian fitting within the energy range of 10–18 MeV for ^{142,148}Nd and 10–19 MeV for ^{146,150}Nd. Figure 8 presents the results of the fitting, while Tables II and III list the corresponding fitting parameters for the LE and HE components, respectively. The Lorentzian fitting was carried out using the χ^2 minimization approach, allowing all parameters to vary freely. The EWSR strengths are evaluated over the excitation-energy range $E_x = 10$–22 MeV for both the LE component (represented by blue lines in Fig. 8) and the HE component (represented by black lines in Fig. 8) in ^{146,148,150}Nd. However, for ^{142}Nd, only the HE component is present as expected since the ^{142}Nd is not deformed. The uncertainties in the strength distributions were derived from the MDA and are reflected as error bars. Since these uncertainties are not purely statistical, the choice of the Lorentzian fitting range significantly affects the errors in the fitting parameters. The quoted uncertainties obtained from the Lorentzian fitting include a 68% confidence interval. The results are compared with the QRPA calculations with the SkM* energy density functional [25] for both the LE and HE components in Tables II and III, respectively.

For the deformed ^{146,148,150}Nd isotopes, the peak position of the LE component aligns with the $K = 0$ component of the ISGQR within the error bars (see Table II and Table VII), indicating the onset of monopole-quadrupole coupling as deformation increases. The EWSR fractions were determined by integrating $E_x S_0(E_x)$ over the 10- to 22-MeV energy range for both the LE and HE components, where S_0 was estimated from the Lorentzian fits. The uncertainties in %EWSR values arise from the errors in the Lorentzian fitting parameters. The EWSR of the LE peak increases with increasing deformation, while the EWSR of the HE peak remains largely unchanged, with a slight decrease observed in ^{146}Nd. This may be due to the transitional nature of the ^{146}Nd nucleus when going from the spherical shape of ^{142}Nd to the prolate-deformed shapes of ^{148}Nd and ^{150}Nd. A similar trend has also been observed in Sm isotopes [16]. At high excitation energies, a nearly constant monopole strength is observed in ^{148}Nd and ^{150}Nd, likely originating from physical continuum effects such as knockout reactions and quasifree processes [3]. The peak positions of the LE and HE components in the ISGMR strength distributions of Nd isotopes agree within error bars with a previous measurement conducted at a significantly lower α beam energy of 129 MeV [22]. The ISGMRs in Nd isotopes have also been studied using the QRPA calculations with different Skyrme energy density functionals, namely SkM* [25], SV-bas, and SkP [52], yielding results consistent with our measured peak positions [21]. Table IV presents the moment ratios $\sqrt{m_3/m_1}$, m_1/m_0, and $\sqrt{m_1/m_{-1}}$ for the

TABLE II. The parameters obtained from Lorentzian fitting of the LE peak of the ISGMR strength distributions in Nd isotopes are presented. The peak energy and width of the LE component are denoted as $E_{\rm LE}$ and $\Gamma_{\rm LE}$, respectively. The uncertainties in the peak energy and width correspond to a 68% confidence interval. The corresponding EWSR values are also presented. For comparison, theoretical values for the excitation energies and widths of the strength distributions are included from Ref. [25].

Isotope	$E_{\rm LE}$ (MeV)	$\Gamma_{\rm LE}$ (MeV)	%EWSR$_{\rm LE}$	$E_{\rm LE}^{\rm theory}$ (MeV)	$\Gamma_{\rm LE}^{\rm theory}$ (MeV)
^{142}Nd	–	–	–	–	–
^{146}Nd	11.5 ± 0.4	3.0 ± 0.8	$17.6^{+9.2}_{-7.4}$	12.1	2.37
^{148}Nd	11.5 ± 0.5	3.5 ± 1.2	$19.1^{+12.7}_{-9.7}$	11.9	2.83
^{150}Nd	12.2 ± 0.4	3.8 ± 1.0	$27.6^{+13.3}_{-10.9}$	11.8	3.22

TABLE III. The parameters obtained from Lorentzian fitting of the HE peak of the ISGMR strength distributions in Nd isotopes are presented. The peak energy and width of the HE component are denoted as $E_{\rm HE}$ and $\Gamma_{\rm HE}$, respectively. The uncertainties in the peak energy and width correspond to a 68% confidence interval. The corresponding EWSR values are also presented. For comparison, theoretical values for the excitation energies and widths of the strength distributions are included from Ref. [25].

Isotope	$E_{\rm HE}$ (MeV)	$\Gamma_{\rm HE}$ (MeV)	%EWSR$_{\rm HE}$	$E_{\rm HE}^{\rm theory}$ (MeV)	$\Gamma_{\rm HE}^{\rm theory}$ (MeV)
^{142}Nd	15.3 ± 0.1	3.3 ± 0.2	$103.9^{+10.9}_{-14.3}$	15.0	2.67
^{146}Nd	15.3 ± 0.2	3.0 ± 0.3	$67.8^{+12.0}_{-11.2}$	14.8	3.05
^{148}Nd	15.2 ± 0.2	4.3 ± 0.4	$108.0^{+15.9}_{-15.2}$	15.0	3.05
^{150}Nd	15.6 ± 0.2	4.0 ± 0.4	$90.9^{+14.4}_{-13.7}$	15.6	3.15

ISGMR strength distributions, derived from Lorentzian fits to the monopole strengths (depicted by red lines in Fig. 8). These ratios are computed over the energy range of 10–22 MeV for each Nd isotope. A decreasing trend is observed from ^{142}Nd to ^{146}Nd, followed by a slight increase toward ^{150}Nd, deviating from the conventional $A^{-1/3}$ rule. This deviation may be attributed to the pronounced deformed nature of ^{150}Nd. The behavior of moment ratios across different deformed isotope chains remain unexplored and necessitates further study.

The ratio of the EWSR exhausted by the HE and LE peaks in ^{150}Nd is 3.3 ± 1.6, indicating a weaker coupling between the ISGMR and ISGQR. A similar value of 4.1 ± 1.2 was reported in Ref. [16] for ^{154}Sm from an experiment conducted at RCNP using an α beam of approximately 400 MeV. Theoretical calculation with the SkP functional for ^{154}Sm yields a ratio of 3.2 [25]. In contrast, α inelastic scattering at 240 MeV, performed by Youngblood *et al.* [17] at TAMU, reports a lower ratio of 2.5 ± 0.2 for ^{154}Sm, suggesting a stronger ISGMR-ISGQR coupling. This discrepancy between the two datasets may arise from differences in the α beam energy [52].

B. ISGDR

The extracted strength distribution for the ISGDR is presented in Fig. 9. The transition operator for dipole transitions is given as follows:

$$O^{1\mu} = \frac{Z}{2A} \sum_k r_k^3 Y_1^\mu(\hat{r_k}), \tag{18}$$

where $Y_1^\mu(\hat{r}_k)$ is the spherical harmonics of order $L = 1$ and μ is the projection of L. This is also a second-order expansion (overtone mode) of the spherical Bessel function since the first-order term refers to the translational motion of the center of mass of the nucleus. This distribution exhibits two distinct peaks: a $1\hbar\omega$ component and a $3\hbar\omega$ component. The $1\hbar\omega$ mode is situated below 10 MeV ($E_x = 30A^{-1/3}$), as reported in Ref. [53]. Nevertheless, the restricted acceptance of the spectrometer leads to a scarcity of data below 10 MeV. The remaining strength distribution displays a clear bimodal behavior, consistent with previous measurements [16,28]. The HE component predominantly covers the 16- to 30-MeV range, while the LE component is largely confined to 10–16 MeV. The nature of the LE peak at 14 MeV remains not fully understood, with suggestions attributing it to "toroidal" [54–56] or "vortex" modes [57,58]. The HE and LE peaks

TABLE IV. The moment ratios in MeV of the ISGMR strength distributions in the Nd isotopes are presented. The uncertainties in the moment ratios were obtained using standard error propagation formulas.

Isotope	$\sqrt{m_3/m_1}$	m_1/m_0	$\sqrt{m_1/m_{-1}}$
^{142}Nd	16.12 ± 0.70	15.66 ± 1.35	15.49 ± 0.68
^{146}Nd	15.60 ± 0.82	14.99 ± 1.48	14.78 ± 0.73
^{148}Nd	15.92 ± 0.82	15.24 ± 1.37	15.00 ± 0.67
^{150}Nd	15.99 ± 0.76	15.32 ± 1.32	15.09 ± 0.65

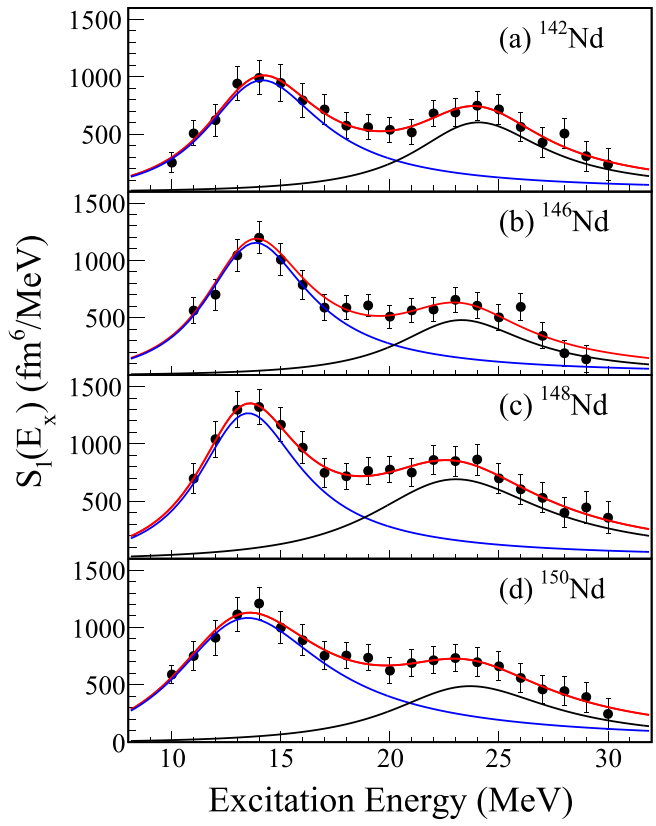

FIG. 9. The ISGDR strength distributions for $^{142-150}$Nd extracted using MDA. The double-Lorentzian fit results are represented by the red line. The blue line indicates the LE component and the black line represents the HE component of the bimodal distributions.

TABLE V. Lorentzian-fit parameters of the LE peak of the bimodal ISGDR strength distributions for the Nd isotopes. The centroid and width are denoted as $E_{\rm LE}$ and $\Gamma_{\rm LE}$, respectively. The uncertainties in the peak energy and width correspond to a 68% confidence interval. The corresponding EWSR values are also presented. For comparison, theoretical values for the excitation energies and widths of the strength distributions are included from Ref. [25].

Isotope	$E_{\rm LE}$ (MeV)	$\Gamma_{\rm LE}$ (MeV)	%EWSR$_{\rm LE}$	$E_{\rm LE}^{\rm theory}$ (MeV)	$\Gamma_{\rm LE}^{\rm theory}$ (MeV)
^{142}Nd	14.1 ± 0.3	6.4 ± 0.5	$51.3^{+3.1}_{-3.6}$	14.2	7.62
^{146}Nd	13.9 ± 0.2	5.9 ± 0.4	$57.9^{+3.7}_{-4.0}$	13.8	8.90
^{148}Nd	13.5 ± 0.2	5.8 ± 0.4	$66.9^{+4.9}_{-5.2}$	13.8	9.26
^{150}Nd	13.5 ± 0.3	8.3 ± 0.6	$63.8^{+3.5}_{-3.8}$	13.7	11.3

are accurately described within the 10- to 30-MeV range by a double Lorentzian function. The form of the Lorentzian function is defined in Eq. (17). The peak values of the LE and HE components shift toward lower excitation energies as nuclear ground-state deformation increases from ^{142}Nd to ^{150}Nd. Additionally, the widths of both LE and HE components broaden with increasing deformation. As discussed in Refs. [25,30], this broadening is further enhanced due to the coupling of the ISGDR with the $K = 0$ and 1 components of the HEOR. The present results for the LE peak have been compared with QRPA calculations with the SkM* energy density functional [25] in Table V. Unlike the theoretically calculated ISGDR strength distribution, which shows the further splitting of the HE component with increasing deformation [25], no such splitting is observed in the present analysis, consistent with the findings in Ref. [16]. Therefore, for the HE peak, the theoretically calculated ISGDR strength distributions are fitted with a single Lorentzian function in the energy range of 18–35 MeV and compared with the present results in Table VI. Values for ^{142}Nd from Ref. [25] have been reported without Lorentzian fitting, as there was no splitting observed in the HE peak of the theoretically calculated ISGDR strength distribution for this isotope.

C. ISGQR

The strength distribution of the ISGQR is shown in Fig. 10. The transition operators for multipoles with $L \geqslant 2$ are expressed as [59]:

$$O^{L\mu} = \frac{Z}{A} \sum_k r_k^L Y_L^\mu(\hat{r}_k), \tag{19}$$

where $Y_L^\mu(\hat{r}_k)$ is the spherical harmonics of order L and μ is the projection of L. This represents the first-order (main-tone) term of the spherical Bessel function, unlike the monopole and dipole modes. The frequency of this main-tone mode is $2\hbar\omega$. The ISGQR strength distributions are fitted using a double Lorentzian fitting function [see Eq. (17)] over the excitation-energy region from 10 to 30 MeV. The fitting results for $^{142-150}$Nd are summarized in Table VII and compared with QRPA calculations [25]. The width of the ISGQR main-tone mode increases with increasing nuclear deformation, attributed to K splitting into $K = 0$, 1, and 2 components [25]. Notably, the LE component of the ISGMR and the main-tone of the ISGQR appear in the same energy region within experimental uncertainties.

A prominent $L = 2$ peak having a frequency of $(4\hbar\omega)$ appears at high excitation energy (26 MeV) in the ISGQR strength distribution (Fig. 10), indicating the presence of the overtone mode of the ISGQR in the Nd isotopes [21]. This overtone mode exhibits a compressional character, similar to the ISGMR and ISGDR. The strength distributions for both the main-tone and overtone modes were obtained using the operator defined in Eq. (19). Continuum random-phase approximation calculations predict the centroid of the overtone mode above 30 MeV [60], which is beyond the reach of the present experimental data. Moreover, at higher excitation energies, contributions from various multipole excitations, knock-out, and quasifree processes dominate, complicating the identification of the overtone mode. In Refs. [60–62], an operator of the form $r^4 - \eta_L r^2$ was used to extract the overtone strength distribution, resulting in a broader peak shifted to higher energies compared to the present findings. The parameter η_L depends on the multipolarities involved. Evidence for the overtone mode in the ISGQR has been suggested in

TABLE VI. Lorentzian-fit parameters of the HE peak of the bimodal ISGDR strength distributions for the Nd isotopes. The centroid and width are denoted as $E_{\rm HE}$ and $\Gamma_{\rm HE}$, respectively. The uncertainties in the peak energy and width correspond to a 68% confidence interval. The corresponding EWSR values are also presented. For comparison, theoretical values for the excitation energies and widths of the strength distributions are included from Ref. [25].

Isotope	$E_{\rm HE}$ (MeV)	$\Gamma_{\rm HE}$ (MeV)	%EWSR$_{\rm HE}$	$E_{\rm HE}^{\rm theory}$ (MeV)	$\Gamma_{\rm HE}^{\rm theory}$ (MeV)
^{142}Nd	24.1 ± 0.4	7.6 ± 1.0	$99.5^{+21.0}_{-20.5}$	26.0	6.32
^{146}Nd	23.3 ± 0.5	6.5 ± 0.9	$76.2^{+14.9}_{-14.6}$	25.3 ± 0.2[a]	7.3 ± 0.5[a]
^{148}Nd	23.0 ± 0.5	9.7 ± 1.2	$131.17^{+17.2}_{-17.8}$	24.5 ± 0.2[a]	10.7 ± 0.7[a]
^{150}Nd	23.7 ± 0.4	9.0 ± 1.1	$89.5^{+14.4}_{-14.6}$	23.3 ± 0.2[a]	14.5 ± 0.8[a]

[a]See text.

TABLE VII. The parameters from the Lorentzian fitting of the ISGQR strength distributions in Nd isotopes are listed. The peak positions and the widths of the main-tone modes, are depicted as $E_{\rm LE}$ and $\Gamma_{\rm LE}$, respectively, while that of the overtone modes, are depicted as $E_{\rm HE}$ and $\Gamma_{\rm HE}$, respectively. A 68% confidence interval has been achieved in the peak positions and widths errors. The corresponding EWSR values are also presented. For comparison, theoretical values for the excitation energies and widths of the strength distributions for the main-tone mode are included from Ref. [25].

	Main-tone mode					Overtone mode		
Isotope	$E_{\rm LE}$ (MeV)	$\Gamma_{\rm LE}$ (MeV)	%EWSR$_{\rm LE}$	$E^{\rm theory}$ (MeV)	$\Gamma^{\rm theory}$ (MeV)	$E_{\rm HE}$ (MeV)	$\Gamma_{\rm HE}$ (MeV)	%EWSR$_{\rm HE}$
^{142}Nd	12.4 ± 0.1	6.3 ± 0.2	$109.6^{+3.5}_{-3.5}$	13.3	2.89	25.5 ± 0.4	10.5 ± 1.3	$78.8^{+7.2}_{-8.0}$
^{146}Nd	12.7 ± 0.1	7.1 ± 0.2	$103.9^{+3.2}_{-3.3}$	12.7	3.01	25.9 ± 0.4	9.3 ± 1.1	$77.8^{+7.1}_{-7.7}$
^{148}Nd	12.2 ± 0.1	6.7 ± 0.2	$104.2^{+4.0}_{-4.1}$	12.6	3.51	25.2 ± 0.6	12.3 ± 2.0	$67.1^{+7.2}_{-8.4}$
^{150}Nd	12.3 ± 0.1	6.9 ± 0.2	$97.5^{+2.5}_{-2.6}$	12.7	4.71	25.7 ± 0.4	8.7 ± 1.1	$70.7^{+7.7}_{-8.4}$

Refs. [31,32] for ^{208}Pb, with further signatures observed in ^{90,92}Zr and ^{92}Mo, indicated by enhanced the ISGQR strength above 20 MeV [51]. However, no QRPA calculations are available to date for the overtone modes in all the Nd isotopes mentioned here. The EWSR fractions were determined by integrating the ISGQR strength distribution over 10–16 MeV for the main-tone mode and 20–30 MeV for the overtone mode.

D. HEOR

The strength distributions for the $L = 3$ excitation are presented in Fig. 11, with the form of the transition operator defined in Eq. (19). The low-energy octupole resonance, however, lies below the acceptance limit of the GR spectrometer, occurring at an excitation energy approximately given by $30A^{-1/3}$ MeV [16,29,63], which corresponds to ∼6 MeV for the Nd isotopes under consideration. In contrast, the HEOR strength distribution spans the 10- to 30-MeV range and is further divided into two distinct regions: a LE component

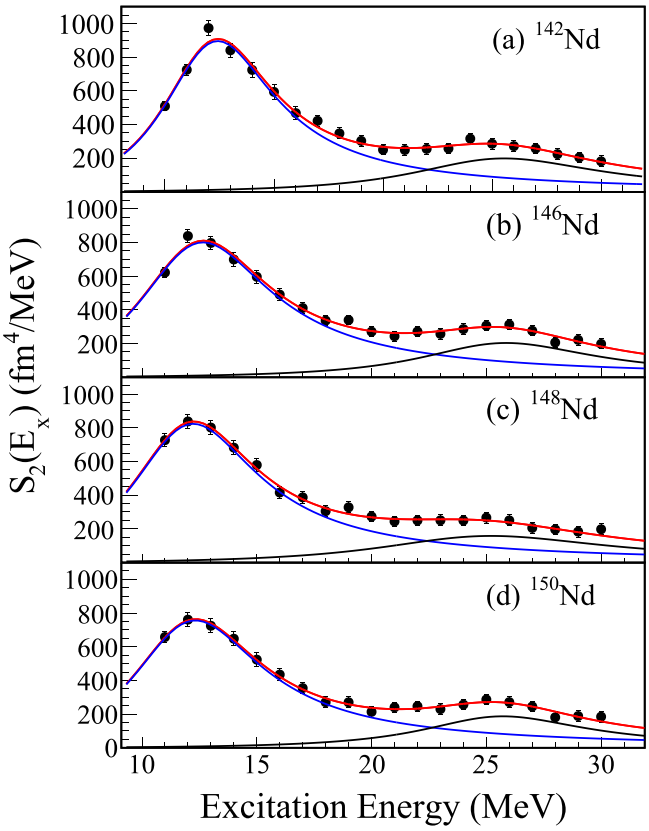

FIG. 10. The ISGQR strength distributions for $^{142-150}$Nd isotopes obtained from the MDA. The overall fits, employing a double-Lorentzian function, are represented by red lines. The main-tone modes of the quadrupole resonances are depicted using blue lines, while the overtone modes are illustrated with black lines.

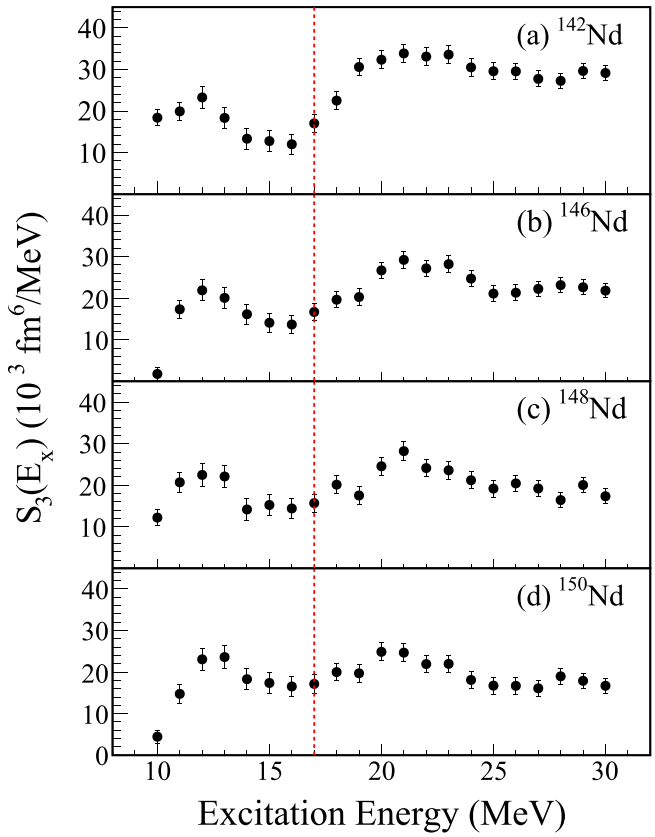

FIG. 11. The $L = 3$ strength distributions for $^{142-150}$Nd isotopes obtained from the MDA. The LE region lies below the red-dashed lines, whereas the HE region of HEOR lies above the red-dashed line.

TABLE VIII. Centroid energies and EWSRs for the HEOR strength distributions in Nd isotopes are listed. For comparison, theoretical values for the excitation energies and widths of the strength distributions are included from Ref. [25].

	LE component		HE component			
Isotope	E_c(LE) (MeV)	%EWSR$_{LE}$	E_c(HE) (MeV)	%EWSR$_{HE}$	E^{theory} (MeV)	EWSR$_{LE}$ / EWSR$_{HE}$
^{142}Nd	12.7 ± 0.7	37.6 ± 5.4	23.2 ± 1.0	197.0 ± 13.2	24.1	0.19
^{146}Nd	13.2 ± 0.7	35.3 ± 5.0	23.1 ± 1.0	155.3 ± 12.5	23.8	0.23
^{148}Nd	12.9 ± 0.7	38.6 ± 5.5	22.9 ± 1.0	136.0 ± 13.2	23.5	0.28
^{150}Nd	13.4 ± 0.7	39.2 ± 5.4	22.8 ± 1.0	126.5 ± 13.1	23.2	0.31

between 10 and 17 MeV and a HE component between 17 and 30 MeV as also seen in Sm isotopes [16]. The corresponding centroid energies (E_c) and percentages of the EWSR for these components were calculated within these ranges and are summarized in Table VIII. Since the HEOR distribution cannot be accurately fitted using a double Lorentzian function, the widths of the strength distributions were not extracted. However, the centroid energies of the LE and HE components were determined by calculating the mean values of the histogram within the specified energy range. The %EWSR is obtained by summing up the fractional EWSR contribution at each energy bin over the defined energy intervals. The centroid energy of the LE component of the HEOR remains the same within uncertainties, in contrast to the findings of Ref. [16] for Sm isotopes. The %EWSRs for the LE components in the 10- to 17-MeV range remain the same within uncertainties. The centroid energies of the HE components in Sm isotopes shift towards lower excitation energies with increasing deformation [16]; such a shift is also observed in Nd isotopes. The %EWSRs for HE components in the 17- to 30-MeV range decrease with increasing nuclear deformation and remain significantly larger than the values reported for Sm isotopes [16]. This discrepancy may stem from the fact that in the present MDA, multipolarities up to $L_{max} = 7$ were considered, whereas, for Sm isotopes, the L_{max} values were 19 for ^{144}Sm and 12 for $^{148-154}$Sm. Furthermore, the nuclear continuum may have significant effects that contribute to the deduced %EWSR. Additionally, the present methodology for determining the %EWSR for HEOR could also result in higher values. However, the %EWSR ratios for the LE and HE components exhibit a trend similar to that observed in Sm isotopes [16]. The peak values for the HE component obtained from QRPA calculations [25] are also listed in Table VIII.

V. SUMMARY

Inelastic α-particle scattering on rare-earth ^{142,146,148,150}Nd isotopes at forward angles was measured using the Grand Raiden spectrometer at RCNP, with a beam energy of approximately 386 MeV. After particle identification, instrumental background subtraction, ion-optical correction, and removal of hydrogen and oxygen contaminants, MDA was employed to extract the strength distributions of giant resonances with various multipolarities. The ISGMR strength distributions exhibit splitting when moving from spherical ^{142}Nd to deformed ^{150}Nd. This splitting arises from the coupling of the ISGMR with the $K = 0$ component of the ISGQR. The extracted ISGMR peak positions align well with previous measurement [22] and with QRPA calculations [25,52]. The ISGDR strength distributions display a bimodal character, with the EWSR of the LE peak increasing alongside nuclear ground-state deformation. The widths of both the LE and HE components of the bimodal distributions broaden with increasing deformation, likely due to coupling with the $K = 0$ and 1 components of the HEOR. For the ISGQR strength distribution, the width of the main-tone peak increases with deformation. A distinct signature of the overtone mode in the ISGQR has also been established, indicating a third type of compression mode beyond the ISGMR and ISGDR. Such an overtone mode of the ISGQR has previously been observed through neutron and proton decay in ^{208}Pb [31,32]. Additionally, the strength distribution of the HEOR mode was extracted, revealing that the EWSR of the HEOR in the 17- to 30-MeV energy range decreases with increasing deformation.

ACKNOWLEDGMENTS

The authors gratefully acknowledge the dedicated staff of the RCNP Ring Cyclotron Facility for providing a high-quality, halo-free α beam. The local support extended by RCNP during the experiment is deeply appreciated. S.B. extends sincere thanks to A. Tamii for assistance in procuring the targets. S.B. is also grateful to the Science and Engineering Research Board (SERB), now known as the Anusandhan National Research Foundation (ANRF), India (Grant No. SRG/2021/000827), and the Faculty Research Scheme at IIT (ISM) Dhanbad [Grant No. FRS(154)/2021-2022/Physics] for financial support. Additionally, S.B. acknowledges GSI Helmholtzzentrum, Germany, for providing travel support to participate in the experiment. M.A. expresses gratitude to IIT (ISM) Dhanbad for the institute fellowship. This work was partially supported by the U.S. National Science Foundation (Grants No. PHY-1713857 and No. PHY-2310059). The isotopes used in this research were supplied by the United States Department of Energy Office of Science by the Isotope Program in the Office of Nuclear Physics.

DATA AVAILABILITY

The data that support the findings of this article are not publicly available. The data are available from the authors upon reasonable request.

[1] M. N. Harakeh and A. van der Woude, *Giant Resonances: Fundamental High Frequency Modes of Nuclear Excitation* (Oxford Science, Oxford, 2001).

[2] S. Shlomo, V. M. Kolomietz, G. Colò, and J. B. Natowitz, Eur. Phys. J. A **30**, 23 (2006).

[3] U. Garg and G. Colò, Prog. Part. Nucl. Phys. **101**, 55 (2018).

[4] S. Stringari, Phys. Lett. B **108**, 232 (1982).

[5] J. R. Stone, N. J. Stone, and S. A. Moszkowski, Phys. Rev. C **89**, 044316 (2014).

[6] G. Giuliani, H. Zheng, and A. Bonasera, Prog. Part. Nucl. Phys. **76**, 116 (2014).

[7] H. A. Bethe, Rev. Mod. Phys. **62**, 801 (1990).

[8] S. E. Woosley, A. Heger, and T. A. Weaver, Rev. Mod. Phys. **74**, 1015 (2002).

[9] A. Burrows, D. Vartanyan, J. Dolence, M. Skinner, and D. Radice, Space Sci. Rev. **214**, 33 (2018).

[10] B. L. Berman and S. C. Fultz, Rev. Mod. Phys. **47**, 713 (1975).

[11] P. Carlos, H. Beil, R. Bergère, A. Leprêtre, and A. Veyssière, Nucl. Phys. A **172**, 437 (1971).

[12] L. Donaldson, C. Bertulani, J. Carter, V. Nesterenko, P. von Neumann-Cosel, R. Neveling, V. Ponomarev, P.-G. Reinhard, I. Usman, P. Adsley, J. Brummer, E. Buthelezi, G. Cooper, R. Fearick, S. Förtsch, H. Fujita, Y. Fujita, M. Jingo, W. Kleinig, C. Kureba *et al.*, Phys. Lett. B **776**, 133 (2018).

[13] L. M. Donaldson, J. Carter, P. von Neumann-Cosel, V. O. Nesterenko, R. Neveling, P.-G. Reinhard, I. T. Usman, P. Adsley, C. A. Bertulani, J. W. Brümmer, E. Z. Buthelezi, G. R. J. Cooper, R. W. Fearick, S. V. Förtsch, H. Fujita, Y. Fujita, M. Jingo, N. Y. Kheswa, W. Kleinig, C. O. Kureba *et al.*, Phys. Rev. C **102**, 064327 (2020).

[14] H. Quliyev, E. Guliyev, and A. A. Kuliev, Nucl. Phys. A **1014**, 122239 (2021).

[15] M. Itoh, H. Sakaguchi, M. Uchida, T. Ishikawa, T. Kawabata, T. Murakami, H. Takeda, T. Taki, S. Terashima, N. Tsukahara, Y. Yasuda, M. Yosoi, U. Garg, M. Hedden, B. Kharraja, M. Koss, B. K. Nayak, S. Zhu, H. Fujimura, M. Fujiwara *et al.*, Phys. Lett. B **549**, 58 (2002).

[16] M. Itoh, H. Sakaguchi, M. Uchida, T. Ishikawa, T. Kawabata, T. Murakami, H. Takeda, T. Taki, S. Terashima, N. Tsukahara, Y. Yasuda, M. Yosoi, U. Garg, M. Hedden, B. Kharraja, M. Koss, B. K. Nayak, S. Zhu, H. Fujimura, M. Fujiwara *et al.*, Phys. Rev. C **68**, 064602 (2003).

[17] D. H. Youngblood, Y.-W. Lui, H. L. Clark, B. John, Y. Tokimoto, and X. Chen, Phys. Rev. C **69**, 034315 (2004).

[18] S. Brandenburg, R. De Leo, A. G. Drentje, M. N. Harakeh, H. Janszen, and A. van der Woude, Phys. Rev. Lett. **49**, 1687 (1982).

[19] Y. K. Gupta, U. Garg, J. Matta, D. Patel, T. Peach, J. Hoffman, K. Yoshida, M. Itoh, M. Fujiwara, K. Hara, H. Hashimoto, K. Nakanishi, M. Yosoi, H. Sakaguchi, S. Terashima, S. Kishi, T. Murakami, M. Uchida, Y. Yasuda, and M. N. Harakeh, Phys. Lett. B **748**, 343 (2015).

[20] T. Peach, U. Garg, Y. K. Gupta, J. Hoffman, J. T. Matta, D. Patel, P. V. Madhusudhana Rao, K. Yoshida, M. Itoh, M. Fujiwara, K. Hara, H. Hashimoto, K. Nakanishi, M. Yosoi, H. Sakaguchi, S. Terashima, S. Kishi, T. Murakami, M. Uchida, Y. Yasuda *et al.*, Phys. Rev. C **93**, 064325 (2016).

[21] M. Abdullah, S. Bagchi, M. N. Harakeh, H. Akimune, D. Das, T. Doi, L. M. Donaldson, Y. Fujikawa, M. Fujiwara, T. Furuno, U. Garg, Y. K. Gupta, K. B. Howard, Y. Hijikata, K. Inaba, S. Ishida, M. Itoh, N. Kalantar-Nayestanaki, D. Kar, T. Kawabata *et al.*, Phys. Lett. B **855**, 138852 (2024).

[22] U. Garg, P. Bogucki, J. D. Bronson, Y.-W. Lui, and D. H. Youngblood, Phys. Rev. C **29**, 93 (1984).

[23] U. Garg, P. Bogucki, J. D. Bronson, Y. W. Lui, C. M. Rozsa, and D. H. Youngblood, Phys. Rev. Lett. **45**, 1670 (1980).

[24] T. Kishimoto, J. M. Moss, D. H. Youngblood, J. D. Bronson, C. M. Rozsa, D. R. Brown, and A. D. Bacher, Phys. Rev. Lett. **35**, 552 (1975).

[25] K. Yoshida and T. Nakatsukasa, Phys. Rev. C **88**, 034309 (2013).

[26] M. Uchida, H. Sakaguchi, M. Itoh, M. Yosoi, T. Kawabata, H. Takeda, Y. Yasuda, T. Murakami, T. Ishikawa, T. Taki, N. Tsukahara, S. Terashima, U. Garg, M. Hedden, B. Kharraja, M. Koss, B. K. Nayak, S. Zhu, M. Fujiwara, H. Fujimura *et al.*, Phys. Lett. B **557**, 12 (2003).

[27] D. H. Youngblood, Y.-W. Lui, B. John, Y. Tokimoto, H. L. Clark, and X. Chen, Phys. Rev. C **69**, 054312 (2004).

[28] B. K. Nayak, U. Garg, M. Hedden, M. Koss, T. Li, Y. Liu, P. V. Madhusudhana Rao, S. Zhu, M. Itoh, H. Sakaguchi, H. Takeda, M. Uchida, Y. Yasuda, M. Yosoi, H. Fujimura, M. Fujiwara, K. Hara, T. Kawabata, H. Akimune, and M. N. Harakeh, Phys. Lett. B **637**, 43 (2006).

[29] H. P. Morsch, M. Rogge, P. Turek, P. Decowski, L. Zemło, C. Mayer-Böricke, S. A. Martin, G. P. A. Berg, I. Katayama, J. Meissburger, J. G. M. Römer, J. Reich, P. Wucherer, and W. Bräutigam, Phys. Lett. B **119**, 311 (1982).

[30] S. Nishizaki and K. Andó, Prog. Theor. Phys. **73**, 889 (1985).

[31] M. Hunyadi, A. van den Berg, N. Blasi, C. Bäumer, M. Csatlós, L. Csige, B. Davids, U. Garg, J. Gulyás, M. N. Harakeh, M. A. de Huu, B. C. Junk, A. Krasznahorkay, S. Rakers, D. Sohler, and H. J. Wörtche, Phys. Lett. B **576**, 253 (2003).

[32] M. Hunyadi, A. M. van den Berg, B. Davids, M. N. Harakeh, M. A. de Huu, H. J. Wörtche, M. Csatlós, J. Gulyás, A. Krasznahorkay, D. Sohler, U. Garg, M. Fujiwara, and N. Blasi, Phys. Rev. C **75**, 014606 (2007).

[33] National nuclear data center (NNDC), https://www.nndc.bnl.gov.

[34] A. Tamii, Y. Fujita, H. Matsubara, T. Adachi, J. Carter, M. Dozono, H. Fujita, K. Fujita, H. Hashimoto, K. Hatanaka, T. Itahashi, M. Itoh, T. Kawabata, K. Nakanishi, S. Ninomiya, A. B. Perez-Cerdan, L. Popescu, B. Rubio, T. Saito, and J. Zenhiro, Nucl. Instrum. Methods A **605**, 326 (2009).

[35] M. Fujiwara, H. Akimune, I. Daito, H. Fujimura, Y. Fujita, K. Hatanaka, H. Ikegami, I. Katayama, K. Nagayama, N. Matsuoka, S. Morinobu, T. Noro, M. Yoshimura, H. Sakaguchi, Y. Sakemi, A. Tamii, and M. Yosoi, Nucl. Instrum. Methods A **422**, 484 (1999).

[36] D. Das, M.Sc. thesis, IIT ISM Dhanbad, 2021.

[37] P. D. Kunz, Program CHUCK3, University of Colorado (1978).

[38] T. Li, U. Garg, Y. Liu, R. Marks, B. K. Nayak, P. V. Madhusudhana Rao, M. Fujiwara, H. Hashimoto, K. Kawase, K. Nakanishi, S. Okumura, M. Yosoi, M. Itoh, M. Ichikawa, R. Matsuo, T. Terazono, M. Uchida, T. Kawabata, H. Akimune, Y. Iwao *et al.*, Phys. Rev. Lett. **99**, 162503 (2007).

[39] K. B. Howard, U. Garg, M. Itoh, H. Akimune, S. Bagchi, T. Doi, Y. Fujikawa, M. Fujiwara, T. Furuno, M. N. Harakeh, Y. Hijikata, K. Inaba, S. Ishida, N. Kalantar-Nayestanaki, T. Kawabata, S. Kawashima, K. Kitamura, N. Kobayashi, Y. Matsuda, A. Nakagawa *et al.*, Phys. Lett. B **801**, 135185 (2020).

[40] S. Bagchi, J. Gibelin, M. N. Harakeh, N. Kalantar-Nayestanaki, N. L. Achouri, H. Akimune, B. Bastin, K. Boretzky, H. Bouzomita, M. Caamaño, L. Càceres, S. Damoy, F. Delaunay, B. Fernández-Domínguez, M. Fujiwara, U. Garg, G. Grinyer, O. Kamalou, E. Khan, A. Krasznahorkay *et al.*, Phys. Lett. B **751**, 371 (2015).
[41] B. Pritychenko, M. Birch, B. Singh, and M. Horoi, At. Data Nucl. Data Tables **107**, 1 (2016).
[42] R. Spear, At. Data Nucl. Data Tables **42**, 55 (1989).
[43] T. Kawabata (private communication).
[44] M. Itoh (private communication).
[45] G. R. Satchler, Nucl. Phys. A **472**, 215 (1987).
[46] M. N. Harakeh and A. E. L. Dieperink, Phys. Rev. C **23**, 2329 (1981).
[47] A. Bohr and B. R. Mottelson, *Nuclear Structure*, Vol. II (W. A. Benjamin, Reading, MA, 1975).
[48] A. Krasznahorkay, J. Bacelar, J. A. Bordewijk, S. Brandenburg, A. Buda, G. van 't Hof, M. A. Hofstee, S. Kato, T. D. Poelhekken, S. Y. van der Werf, A. van der Woude, M. N. Harakeh, and N. Kalantar-Nayestanaki, Phys. Rev. Lett. **66**, 1287 (1991).
[49] V. Plujko, O. Gorbachenko, R. Capote, and P. Dimitriou, At. Data Nucl. Data Tables **123-124**, 1 (2018).
[50] E. Lipparini and S. Stringari, Phys. Rep. **175**, 103 (1989).
[51] Y. K. Gupta, K. B. Howard, U. Garg, J. T. Matta, M. Şenyiğit, M. Itoh, S. Ando, T. Aoki, A. Uchiyama, S. Adachi, M. Fujiwara, C. Iwamoto, A. Tamii, H. Akimune, C. Kadono, Y. Matsuda, T. Nakahara, T. Furuno, T. Kawabata, M. Tsumura *et al.*, Phys. Rev. C **97**, 064323 (2018).
[52] J. Kvasil, V. O. Nesterenko, A. Repko, W. Kleinig, and P.-G. Reinhard, Phys. Rev. C **94**, 064302 (2016).
[53] T. D. Poelhekken, S. K. B. Hesmondhalgh, H. J. Hofmann, H. W. Wilschut, A. van der Woude, and M. N. Harakeh, Phys. Lett. B **278**, 423 (1992).
[54] D. Vretenar, N. Paar, P. Ring, and G. A. Lalazissis, Nucl. Phys. A **692**, 496 (2001).
[55] E. B. Balbutsev, I. V. Molodtsova, and A. V. Unzhakova, Europhys. Lett. **26**, 499 (1994).
[56] N. Paar, D. Vretenar, E. Khan, and G. Colò, Rep. Prog. Phys. **70**, R02 (2007).
[57] J. Kvasil, V. O. Nesterenko, W. Kleinig, P.-G. Reinhard, and P. Vesely, Phys. Rev. C **84**, 034303 (2011).
[58] P.-G. Reinhard, V. O. Nesterenko, A. Repko, and J. Kvasil, Phys. Rev. C **89**, 024321 (2014).
[59] A. M. Bernstein, Adv. Nucl. Phys. **3**, 325 (1969).
[60] M. L. Gorelik, I. V. Safonov, and M. H. Urin, Phys. Rev. C **69**, 054322 (2004).
[61] M. L. Gorelik, S. Shlomo, B. A. Tulupov, and M. H. Urin, Phys. Rev. C **103**, 034302 (2021).
[62] M. L. Gorelik, S. Shlomo, B. A. Tulupov, and M. H. Urin, Phys. Rev. C **108**, 014328 (2023).
[63] H. L. Clark, D. H. Youngblood, and Y.-W. Lui, Phys. Rev. C **54**, 72 (1996).